

# The Impact of 2022 Hunga Tonga-Hunga Ha'apai (Hunga) Eruption on Stratospheric Circulation and Climate

Simchan Yook<sup>1\*</sup>, Susan Solomon<sup>1</sup>, and Xinyue Wang<sup>2</sup>

## Affiliations:

<sup>1</sup> Department of Earth, Atmospheric and Planetary Sciences, Massachusetts Institute of Technology, Cambridge, MA, USA

<sup>2</sup> Department of Atmospheric and Oceanic Sciences, University of Colorado Boulder, Boulder, CO, USA

\* Corresponding author. Email: [syook@mit.edu](mailto:syook@mit.edu)

## Key Points:

- Simulated climate responses to the Hunga eruption based on specified-chemistry runs show good agreement with previous coupled-chemistry runs
- Ozone, water vapor, and aerosol from the Hunga eruption each contributed to the circulation and temperature anomalies in the stratosphere
- The simulated springtime ozone anomalies contributed to the temperature anomalies in the Southern Hemisphere lower stratosphere during winter 2022

21 Abstract:

22 The Hunga Tonga-Hunga Ha'apai (Hunga) volcanic eruption in January 2022 injected a  
23 substantial amount of water vapor and a moderate amount of SO<sub>2</sub> into the stratosphere. Both  
24 satellite observations in 2022 and subsequent chemistry-climate model simulations forced by  
25 realistic Hunga perturbations reveal large-scale cooling in the Southern Hemisphere (SH)  
26 tropical to subtropical stratosphere following the Hunga eruption. This study analyzes the drivers  
27 of this cooling, including the distinctive role of anomalies in water vapor, ozone, and sulfate  
28 aerosol concentration on the simulated climate response to the Hunga volcanic forcing, based on  
29 climate simulations with prescribed chemistry/aerosol. Simulated circulation and temperature  
30 anomalies based on specified-chemistry simulations show good agreement with previous  
31 coupled-chemistry simulations and indicate that each forcing of ozone, water vapor, and sulfate  
32 aerosol from the Hunga volcanic eruption contributed to the circulation and temperature  
33 anomalies in the Southern Hemisphere stratosphere. Our results also suggest that 1) the large-  
34 scale stratospheric cooling during the austral winter was mainly induced by changes in  
35 dynamical processes, not by radiative processes, and that 2) the radiative feedback from negative  
36 ozone anomalies contributed to the prolonged cold temperature anomalies in the lower  
37 stratosphere (~70 hPa level) and hence to long lasting cold conditions of the polar vortex.

38

39 **Plain Language Summary**

40 In January 2022, the Hunga Tonga-Hunga Ha'apai (Hunga) volcanic eruption injected large  
41 amounts of water vapor and moderate amounts of sulfur dioxide into the stratosphere. Previous  
42 observational and modeling studies show that this injection led to decreases in stratospheric  
43 temperature. We use a climate model forced with prescribed chemical composition from the  
44 Hunga eruption to explore how the changes in water vapor, ozone, and sulfate aerosols affected

45 stratospheric climate. Our findings confirm that these forcings all contributed to the changes in  
46 temperatures and circulation in the Southern Hemisphere's stratosphere. The cooling during  
47 austral winter was mainly due to changes in atmospheric dynamics rather than direct radiative  
48 effects, but the ozone's radiative feedback also contributed to sustaining the cold temperature  
49 anomalies in the lower stratosphere in late spring.

50

51

52

53

54

55

56

57

58

59

60

61

62

63

64

65

66

67

68 **Main Text:**

69 **1. Introduction**

70 The Hunga Tonga-Hunga Ha'apai (Hunga) volcanic eruption (21°S, 175°W) was one of the  
71 most explosive eruptions observed since satellite era. Observations reveal that the Hunga  
72 eruption injected a substantial amount of water vapor (>150 Tg) into the stratosphere, resulting  
73 in a ~10% increase in the stratospheric water vapor burden (Khaykin et al., 2022; Millán et al.,  
74 d2022; Vömel et al., 2022), which was unprecedented in the available observational record. The  
75 Hunga eruption also injected a moderate amount of SO<sub>2</sub> (~0.4-0.5 Tg) into the stratosphere (Carn  
76 et al., 2022; Taha et al., 2022; Witze, 2022; Sellitto et al., 2022). The injected SO<sub>2</sub> was quickly  
77 converted to sulfate aerosol particles through oxidation, which was accelerated by the excessive  
78 moisture (Zhu et al., 2022; Wang et al., 2023; Asher et al., 2023).

79 Many studies have explored the impacts of the Hunga water vapor and aerosol perturbations  
80 on stratospheric temperatures, circulation and chemistry. Both satellite observations in 2022 and  
81 subsequent model simulations forced by realistic Hunga perturbations reveal large-scale cooling  
82 in the Southern Hemisphere (SH) tropical to subtropical stratosphere, large mesospheric  
83 temperature anomalies (Yu et al., 2023), a strengthening and equatorward shift of the  
84 stratospheric polar night jet, and a weaker stratospheric overturning circulation (Coy et al., 2022;  
85 Schoeberl et al., 2022; Wang et al., 2023; Fleming et al., 2024). Substantial ozone reduction was  
86 also observed in the mid-stratosphere over SH mid-latitudes during austral winter and over polar  
87 regions during austral spring (Lu et al., 2023; Zhang et al., 2023; Wang et al., 2023). The net  
88 tropospheric radiative forcing from the Hunga perturbations is estimated to be small but negative  
89 due to compensation between a heating linked to the water vapor increase and a cooling due to  
90 the reduction in direct solar flux by the aerosol layer (Schoeberl et al., 2023).

91 The changes in stratospheric composition and circulation in response to the Hunga forcing  
92 evolve through complex interactions in the atmosphere. This complexity makes it challenging to  
93 quantify the exact role of each forcing on climate anomalies in a coupled chemistry-climate  
94 model simulation. For example, the evolution of ozone is simulated through both dynamical and  
95 chemical processes in a coupled chemistry model. The changes in ozone can affect temperatures  
96 and thus circulation through radiative effects, which, in turn, can affect the ozone concentration  
97 again. Thus, in a coupled chemistry simulation, it is difficult to quantify to what extent the  
98 circulation anomalies in 2022 were forced by the ozone perturbations. Additionally, while some  
99 single forcing (e.g., water vapor or SO<sub>2</sub> only) experiments can be conducted in the coupled  
100 chemistry-climate setting to separate the role of each Hunga volcanic forcing on the climate  
101 responses, they require assumptions that any differences in the evolution of water vapor and SO<sub>2</sub>  
102 among different experiments are negligible. Thus, making a precise attribution of each forcing  
103 on the circulation anomalies in the coupled chemistry simulation is difficult.

104 Wang et al. (2023) conducted comprehensive analyses using coupled chemistry-climate  
105 simulations forced by realistic Hunga inputs of H<sub>2</sub>O and SO<sub>2</sub>. Their simulations successfully  
106 reproduced the observed changes in temperature, circulation, and ozone, demonstrating how the  
107 Hunga forcing contributed to the stratospheric climate anomalies and ozone losses in 2022. Here  
108 we conduct further analysis aimed at identifying the contribution of each individual forcing term  
109 that contributes to those climate anomalies: ozone, water vapor, and aerosols, respectively. To do  
110 so, we ran a series of numerical experiments using the “Specified Chemistry” (SC) version of the  
111 Whole Atmosphere Community Climate Model (WACCM; Gettelman et al., 2019) forced with  
112 prescribed chemical composition from the previous “Free Running” (FR) WACCM simulations  
113 by Wang et al. (2023).

114

115 **2. Method**

116 **2.1. SC-WACCM**

117 To isolate the circulation responses to the Hunga perturbations from the coupled  
118 chemistry-climate interactions, we used the SC version of the WACCM (SC-WACCM; Smith et  
119 al., 2014). The SC-WACCM simulations were run with a horizontal resolution of  $1.25^\circ \times 0.9^\circ$ ,  
120 70 vertical levels, and a model top at about 140 km. The model was coupled to interactive ocean,  
121 land, and sea ice models.

122 The SC-WACCM simulation is essentially identical to the FR-WACCM simulation  
123 except that the chemical composition of the middle atmosphere is prescribed as data, rather than  
124 calculated by the model (details described in Smith et al., 2014). SC-WACCM simulates only the  
125 radiative effects of prescribed concentrations of gases and aerosols on the temperature fields, but  
126 not the influence of dynamical fields on the chemical species. Thus, using SC-WACCM, we can  
127 estimate the circulation responses to specified amounts of gas and aerosol perturbations in a  
128 consistent manner across various sets of experiments. For example, sulfate aerosol in the  $\text{SO}_2$ -  
129 only experiment run on the FR-WACCM simulations may not be identical to the aerosol in the  
130 FR-WACCM simulations run with both  $\text{SO}_2$  and  $\text{H}_2\text{O}$  forcing due to differences in the dynamical  
131 and chemical evolution of the sulfate aerosol between the two runs. However, in SC-WACCM,  
132 we can apply the same aerosol forcing for different sets of experiments. Since SC-WACCM does  
133 not involve any calculations of chemical reactions, it can also reduce computational costs to  
134 about half of those for the FR-WACCM, while reproducing similar results in long-term statistics  
135 of climate scale (Smith et al., 2014).

136

137 **2.2. Experiments**

138 We used two sets of FR-WACCM experiments conducted by Wang et al. (2023) to  
139 generate the prescribed chemical composition forcing files and compare the results: 1) **FR-**  
140 **CTRL**, the control case run without the Hunga volcanic forcing, and 2) **FR-ALL**, the perturbed  
141 case run with realistic Hunga forcing. The Hunga volcanic forcing in the **FR-ALL** runs included  
142 the injection of 150 Tg of H<sub>2</sub>O and 0.42 Tg of SO<sub>2</sub> into the stratosphere (for details, see section  
143 2.3 in Wang et al., 2023). In parallel with their FR-WACCM simulations, we performed five sets  
144 of additional SC-WACCM experiments forced with different combinations of prescribed  
145 chemical compositions (water vapor, ozone, and aerosol) as follows:

146 1) **SC-CTRL**, control experiments forced with the water vapor, ozone, and aerosol fields  
147 taken from the **FR-CTRL** runs,

148 2-4) **SC-H2O**, **SC-O3**, and **SC-SULF**, three sets of single forcing experiments forced  
149 with water vapor, ozone, and sulfate aerosol field, respectively, from the **FR-ALL** runs and two  
150 other fields from the **FR-CTRL** runs, and

151 5) **SC-ALL**, all forcing experiments forced with all three fields from the **FR-ALL** runs.

152 The forcing files were generated based on zonal-mean and daily-mean fields from each  
153 ensemble member. We used 10 ensemble members for each set of experiments, each run with  
154 forcing files generated from the corresponding ensemble member of the FR runs, to isolate the  
155 circulation responses to the Hunga forcing from other forms of internal climate variability. All  
156 ensemble members were integrated from January 1, 2022, until December 31, 2022.

157 To reproduce the initial structure and development of the Hunga plume, the modeled  
158 winds and temperatures were relaxed toward reference meteorology from Modern-Era  
159 Retrospective Analysis for Research and Applications version 2 (MERRA2, Gelaro et al., 2017).  
160 Following Wang et al. (2023), in all experiments we adjusted the WACCM wind and  
161 temperature fields to match the MERRA2 data with a relaxation time of 12 hours throughout  
162 January 2022. After February 1, 2022, the model was free-running without any nudging applied.

163 The differences in ensemble mean fields between the forcing and control runs are  
164 explored to estimate the mean climate anomalies in response to the Hunga forcing. The t-statistic  
165 was used to assess the statistical significance of the difference ( $p < 0.05$ ) in mean climate  
166 between two sets of simulations. The main purpose of this study was to examine the climate  
167 response to the chemical forcing derived from the previous FR-WACCM simulations. Thus, we  
168 compared the results from the SC runs with those from the FR runs, rather than with  
169 observations.

170

### 171 **2.3. Ozone Monitor and Profiler Suite Limb Profiler (OMPS-LP)**

172 The ozone anomaly data for 2022 (with respect to the 2012–2021 mean seasonal cycle)  
173 were derived from the Ozone Mapping and Profiler Suite Limb Profiler (OMPS-LP) instrument  
174 (Taha et al., 2021; Zawada et al., 2018). OMPS-LP observations have been employed in multiple  
175 studies investigating the Antarctic ozone hole (Kramarova et al., 2014; Rieger et al., 2021; Yu et  
176 al., 2021; Wang et al., 2023). We note that the OMPS ozone data were used to compare the  
177 modeled evolution of ozone with observations but not used as prescribed forcing in the model  
178 experiments.

179

180 **3. Results**

181 The Hunga perturbations in the **FR-ALL** simulations consist of stratospheric aerosol and  
182 gases that evolve over time following the initial injection of SO<sub>2</sub> and H<sub>2</sub>O into the stratosphere.  
183 Wang et al. (2023) demonstrated that the simulated evolution of the H<sub>2</sub>O and sulfate aerosol  
184 plumes, resulting from the initial perturbations, closely matches the patterns from satellite  
185 observations. We hypothesized that water vapor, ozone, and sulfate aerosol were the main  
186 radiative forcings resulting from the initial injection of the Hunga forcing. Thus, we used the  
187 water vapor, ozone, and sulfate aerosol fields from the **FR-ALL (FR-CTRL)** experiments to  
188 form the prescribed Hunga forcing in the **SC-ALL (SC-CTRL)** experiments.

189 We assess whether the simulated circulation and temperature anomalies from the SC-  
190 WACCM runs, forced with prescribed stratospheric water vapor, ozone, and aerosols, align well  
191 with the results from the FR-WACCM runs. Figure 1 shows the temperature responses (averaged  
192 over 50°S–0°) to the Hunga forcing as differences between the all forcing (**ALL**) runs and the  
193 control (**CTRL**) runs in FR- and SC-WACCM simulations (top and bottom, respectively)..  
194 Consistent with findings from previous studies (Wang et al., 2023; Fleming et al., 2023), the  
195 Hunga perturbations lead to cooling of ~1 K over much of the middle stratosphere above ~30  
196 hPa level, juxtaposed with weaker warming in the lower stratosphere below ~50 hPa throughout  
197 2022, in both the FR and SC runs (Fig. 1). Close similarity in the climate responses to the Hunga  
198 perturbations between the FR and SC runs shown in Fig. 1 suggests that 1) the three forcings in  
199 SC runs effectively represent the net radiative forcing of the Hunga perturbations, and 2) the  
200 simulated SH temperature anomalies in the stratosphere during 2022 are radiative responses to  
201 the Hunga forcing.

202 We next explore the extent to which the climate anomalies in 2022 were affected by each  
203 forcing of ozone, water vapor, and sulfate aerosol from the Hunga eruption. Figure 2 reveals the  
204 temperature anomalies based on the single forcing experiments, **SC-H2O**, **SC-O3**, and **SC-**  
205 **SULF**. The temperature anomalies based on single forcing experiments show that the persistent  
206 cold temperature anomalies above ~30 hPa level are largely due to the water vapor perturbations  
207 (Fig. 2a). This is expected, as the radiative effects of stratospheric water vapor will induce  
208 cooling in the stratosphere (Forster et al., 1999). Wang et al. (2023) also showed that the cold  
209 temperature anomalies overlap with the water vapor plume. The warm temperature anomalies  
210 below the ~30 hPa level result from radiative heating from the volcanic aerosol layer in the lower  
211 stratosphere. These warm anomalies are reinforced by the absorption of upwelling longwave  
212 radiation by the water vapor plume (Figs. 2a and 2c, and also Figure 3 in Wang et al., 2023).

213 In the all forcing (Fig. 1), **SC-O3** (Fig. 2b), and **SC-SULF** (Fig. 2c) runs, the dipole  
214 vertical structure, characterized by cooling above and warming below, becomes less distinct  
215 during the austral winter. Instead, warming features emerge in the **SC-O3** and **SC-SULF** runs  
216 (Figs. 2b-c). Given that cold temperature anomalies are also observed over high latitudes during  
217 austral winter (Figs. 3, 4b, and 4c), the warming pattern over the tropics suggests the well-known  
218 out-of-phase temperature variations between the tropics and extratropics, associated with  
219 changes in the Brewer-Dobson circulation (Yulaeva et al., 1994; Randel et al., 2007; Ueyama  
220 and Wallace, 2010). We infer that the dynamical warming over the tropics partially offsets the  
221 radiative cooling caused by water vapor in all forcing experiments during the winter (Figs. 1, 3a,  
222 and 3b).

223 In the following section, we explore the wintertime circulation and temperature  
224 anomalies. Figure 3 reveals the difference in wintertime (July-August-September) zonal-mean

225 temperature (top) and zonal wind (bottom) between the all forcing (**ALL**) runs and the control  
226 (**CTRL**) runs in (left) FR- and (right) SC-WACCM simulations. The simulated temperature  
227 differences show a cooling pattern in the stratosphere centered at extratropical latitudes  $\sim$ 60°S in  
228 both the FR and SC runs (Figs. 3a-b). The zonal wind anomalies also reveal a strengthening of  
229 the equatorward flank of the winter westerlies in both runs (Figs. 3c-d).

230        However, unlike the substantial cooling pattern that emerges at high latitudes, the water  
231 vapor-driven cooling anomalies at tropical latitudes (above 30 hPa), discussed in the previous  
232 section, become less distinct during August–October in the **SC-ALL** runs (Figs. 1 and 3). Given  
233 that cold temperature anomalies are observed at extratropical latitudes during the austral winter  
234 (Fig. 3), we expect dynamically induced warming over the tropics due to the well-known out-of-  
235 phase temperature variations between the tropics and extratropics, associated with changes in the  
236 Brewer-Dobson circulation (Yulaeva et al., 1994; Randel et al., 2007; Ueyama and Wallace,  
237 2010). The signatures of a warming pattern over the tropics, coupled with the cooling over the  
238 extratropics, are also evident in the **SC-SULF** runs, where the tropical cooling from the water  
239 vapor anomalies is absent (Figs. 2c and 4d). Thus, we infer that the dynamical coupling of  
240 wintertime circulation between the extratropics and tropics induces warming over the tropics  
241 which partially offsets the radiative cooling caused by tropical water vapor forcing in **SC-**  
242 **ALL** runs (Figs. 1 and 3).

243        Figure 4 presents the wintertime circulation anomalies from the three single forcing  
244 experiments, showing the differences between each of the three forcing runs (**SC-H2O**, **SC-O3**,  
245 and **SC-SULF**) and the **SC-CTRL** runs. The single forcing runs exhibit a similar pattern of  
246 wintertime climate anomalies, including cooling of the Antarctic polar vortex and a

247 strengthening of the equatorward flank of the stratospheric polar jet, consistent with the all  
248 forcing runs.

249 The **SC-SULF** runs exhibit the largest zonal wind and temperature anomalies among the  
250 three single-forcing experiments (Fig. 4). Aerosols from large tropical volcanic eruptions can  
251 influence stratospheric temperatures and winds through direct radiative effects (e.g., DallaSanta  
252 et al., 2019; Kodera, 1994; Robock, 2000; Robock & Mao, 1995; Toohey et al., 2014) and  
253 indirect mechanisms (e.g., Coupe & Robock, 2021). Previous modeling studies have also shown  
254 that direct warming in the tropical stratosphere leads to the strengthening of the winter polar  
255 vortex (e.g., DallaSanta et al., 2019; Toohey et al., 2014; Revell et al., 2017). In the **SC-SULF**  
256 runs, warm temperature anomalies are observed in the lower tropical stratosphere due to  
257 radiative heating from the volcanic aerosol layer (Figs. 2c and 4c). Thus, consistent with findings  
258 from other modeling studies, the wintertime climate anomalies in the **SC-SULF** runs indicate the  
259 response to lower tropical warming induced by the aerosol layer (Figs. 4c and 4f).

260 However, we note that the extratropical circulation anomalies in the single-forcing  
261 experiments have much smaller amplitudes compared to those in the all-forcing runs (Figs 3 and  
262 4) and are not statistically significant ( $p > 0.05$ ). Thus, including both water vapor and sulfate  
263 aerosol forcings is expected to be important for a realistic simulation of the Hunga forcing.

264 It is also known that the circulation response can be obscured by the large internal  
265 variability of the stratospheric polar vortex (DallaSanta & Polvani, 2022). Dynamical analyses  
266 based on the FR runs by Yu et al. (2023) and Wang et al. (2023) also suggest a considerable  
267 contribution of stochastic components in the wintertime extratropical circulation response to the  
268 Hunga eruption. Thus, while the similarity between the circulation anomalies in the FR and SC  
269 runs (Fig. 3) provides circumstantial evidence that the wintertime circulation anomalies are

270 likely due to the Hunga eruption, we also note that considerable stochastic variability remains  
271 due to the limited number of available ensemble members.

272 To better understand the wintertime climate responses to the Hunga forcing, the time  
273 series of daily-mean polar cap averaged (60–90°S) temperature anomalies are illustrated in Figure  
274 5. Given the low signal-to-noise ratio observed in the wintertime circulation anomalies from the  
275 single forcing experiments (Fig. 4), we focus on the results based on all forcing experiments. The  
276 vertical structure of the polar cap temperature responses both in the FR and SC runs shows  
277 similar cooling pattern across most of the stratosphere during the austral winter and spring 2022,  
278 with the largest cold anomalies in August–September (Fig. 5). Extratropical winds are in thermal  
279 wind balance with the temperature anomalies. Thus, the pattern of extratropical (30–60°S) zonal  
280 mean zonal wind anomalies is illustrated in Figure 6. The intensification of the extratropical  
281 zonal mean zonal winds is shown throughout the stratosphere during winter, extending into the  
282 lower stratosphere in spring (Fig. 6). We note that the SC runs do not show significant  
283 tropospheric or surface temperature anomalies in 2022 (not shown).

284 We further assess the contribution of radiative and dynamical processes to the simulated  
285 polar cap averaged (60–90°S) temperature anomalies focusing on the results from the SC-  
286 WACCM experiments (**SC-ALL** minus **SC-CTRL**) in Figure 7. The polar cap temperature  
287 anomalies at the upper (5 hPa) and lower (70 hPa) stratospheric levels are decomposed into three  
288 components: shortwave (SW) heating rates, longwave (LW) heating rates, and dynamical  
289 temperature changes, in Figs. 7a and 7b, respectively. The temperature tendencies from different  
290 dynamical and physical processes are derived from the output fields in CESM: DTCORE for  
291 tendency driven by dynamical processes (i.e., the temperature tendency calculated by the  
292 dynamical core), QRL for longwave heating, and QRS for shortwave heating. Other physical

293 processes (e.g., vertical diffusion, gravity wave drag, and moisture processes) also contribute to  
294 temperature changes. However, their effects were negligible in our analyses, which focused on  
295 the differences between the **SC-ALL** and **SC-CTRL** experiments.

296 The results shown in Figure 7 are not time series of temperature tendencies (units: K/sec),  
297 but time-integrated temperature tendencies (units: K) since January 1, 2022. The time integration  
298 of temperature tendencies enables us to directly compare the temperature changes calculated  
299 from each temperature tendency with the temperature anomalies shown in Figure 5. The same  
300 method was used in Zou et al. (2021) for their temperature diagnosis.

301 Cold temperature anomalies in the upper stratosphere begin to develop in early June  
302 (with the onset indicated by the grey line), primarily due to enhanced dynamical cooling,  
303 partially offset by decreased longwave cooling from the reduced Planck feedback (Fig. 7a).  
304 These changes in dynamical temperature tendencies are consistent with findings in previous  
305 studies (Wang et al., 2023; Coy et al., 2022), which indicate that the wintertime circulation  
306 responses to the Hunga forcing are characteristic of dynamically forced effects, including  
307 weakened planetary-scale wave forcing and changes in the residual mean (Brewer-Dobson)  
308 circulation.

309 Interestingly, while dynamical cooling drives the cold temperature anomalies in the lower  
310 stratosphere (70 hPa) during June-November, a comparable amount of negative anomalies in  
311 shortwave heating also contribute to the prolonged cold temperature anomalies during October-  
312 December (Fig. 7b). We identify the source of these SW heating anomalies by comparing the  
313 SW heating anomalies in the all forcing (**SC-ALL**) and ozone-only forcing (**SC-O3**) experiments  
314 in Figure 8. The results from the **SC-ALL** and **SC-O3** runs reveal a consistent pattern of changes  
315 in shortwave heating rates, including substantial negative anomalies in the lower stratosphere

316 during October-December (Figure 6). However, no significant changes in SW heating rates are  
317 observed in the **SC-SULF** and **SC-H2O** runs (not shown). This suggests that the SW heating  
318 anomalies in the lower stratosphere in late spring are largely driven by the radiative effects of  
319 ozone. The results are also consistent with findings from previous studies suggesting that ozone  
320 changes are the primary driver of temperature changes in the lower stratosphere during austral  
321 spring (Calvo et al., 2012; 2017).

322 Figure 9 shows the evolution of springtime polar-cap ozone anomalies in 2022 based on  
323 OMPS observations (top) and simulated ozone from FR-WACCM (bottom). Both the  
324 observations and the WACCM simulations show negative anomalies in polar-cap ozone  
325 concentrations across much of the stratosphere during spring 2022. Zhang et al. (2023) reported  
326 that most of the ozone anomalies in 2022 were primarily driven by circulation anomalies.  
327 However, their findings also show that the chemical loss of ozone was particularly large in the  
328 lower stratosphere during austral spring 2022, accounting for up to ~20% of the Antarctic ozone  
329 loss at 80 hPa in October 2022. Thus, together with the findings from Zhang et al. (2023), the  
330 results in Figs. 8-9 emphasize the role of chemistry-climate interactions in driving climate  
331 anomalies in the lower stratosphere. We note that the occurrence of positive ozone anomalies  
332 above the negative ozone anomalies is consistent with the signatures of dynamical changes  
333 investigated in previous studies (Calvo et al., 2012, 2017).

334

#### 335 **4. Summary and Conclusions**

336 Recent observational and modeling studies explored the stratospheric climate anomalies  
337 following the Hunga volcanic eruption, including influences on the stratospheric temperatures,  
338 chemistry, large-scale circulation, and net radiative forcing (Wang et al., 2023; Coy et al., 2023;

339 Zhang et al., 2023; Lu et al., 2023; Schoeberl et al., 2022, 2023; Fleming et al., 2024). Two  
340 recent studies used the same chemistry-climate model (WACCM) but with different  
341 configurations to address various aspects of the climate responses to the Hunga eruption. Wang  
342 et al. (2023) explored the evolution of stratospheric composition and circulation using a free-  
343 running version of WACCM, while Zhang et al. (2023) focused on changes in stratospheric  
344 chemistry with a specified-dynamics version of WACCM.

345 Here, we extend their method, but focusing on decomposing the contributions of each  
346 forcing — ozone, water vapor, and sulfate aerosol — from the Hunga volcanic eruption to the  
347 simulated stratospheric circulation and temperature anomalies in 2022. To do so, we examined  
348 differences in climate anomalies based on a series of specified-chemistry WACCM experiments  
349 with various configurations of prescribed Hunga forcing.

350 The simulated climate responses to the Hunga forcing based on our specified-chemistry  
351 simulations (**SC-ALL**) show good agreement with previous coupled-chemistry simulations (**FR-**  
352 **ALL**). We find that the large-scale stratospheric cooling that occurred in 2022 austral  
353 winter/early spring (June-December) was mainly driven by changes in dynamical processes and  
354 not by direct radiative forcing. However, a key finding of this paper is that from October to  
355 December 2022, ozone's radiative feedback contributed to the prolonged cold temperature  
356 anomalies in the lower stratosphere ( $\approx 70$  hPa) from October to December 2022 and hence to  
357 long lasting cold conditions of the polar vortex.

358 Together with findings from Wang et al. (2023) and Zhang et al. (2023), our results  
359 highlight that consistent model experiments with different configurations of a single model can  
360 improve our understanding of the climate responses associated with the observed volcanic  
361 eruption event. Our results also highlight some practical implications of using Specified

362 Chemistry setting of WACCM for studying climate and chemistry interactions. The similarity  
363 between the results from the FR and SC runs suggests that the SC runs can effectively estimate  
364 the temperature and circulation responses to the Hunga perturbations, providing a more  
365 computationally efficient alternative to fully coupled chemistry simulations (Smith et al., 2014).  
366 This efficiency makes SC runs useful for isolating the climate response to perturbations in  
367 individual chemical components.

368

369 **Acknowledgments:** S. S and S. Y. are supported by grant AGS-1906719 and AGS- 2316980  
370 from the Atmospheric Chemistry Division of the U.S. National Science Foundation (NSF) as  
371 well as a grant from the Future of Life Institute. The CESM project is supported primarily by the  
372 U.S. National Science Foundation. The authors acknowledge the Climate Simulation Laboratory  
373 at NCAR’s Computational and Information Systems Laboratory (CISL; sponsored by NSF and  
374 other agencies) and the MIT’s Massachusetts Green High Performance Computing Center  
375 (supported by the Center for Sustainability Science and Strategy) for providing computing and  
376 storage resources. We thank William Randel and the three anonymous reviewers for their helpful  
377 comments on the manuscript.

378

379 **Open Research Section**

380 Dataset used in the generation of the figures of this paper are available in Yook (2024).  
381 CESM2/WACCM6 is an open-source community model, which was developed with support  
382 primarily from the National Science Foundation, see Gettelman et al. (2019).

383

384

385

386

387

388

389

390

391

392

393

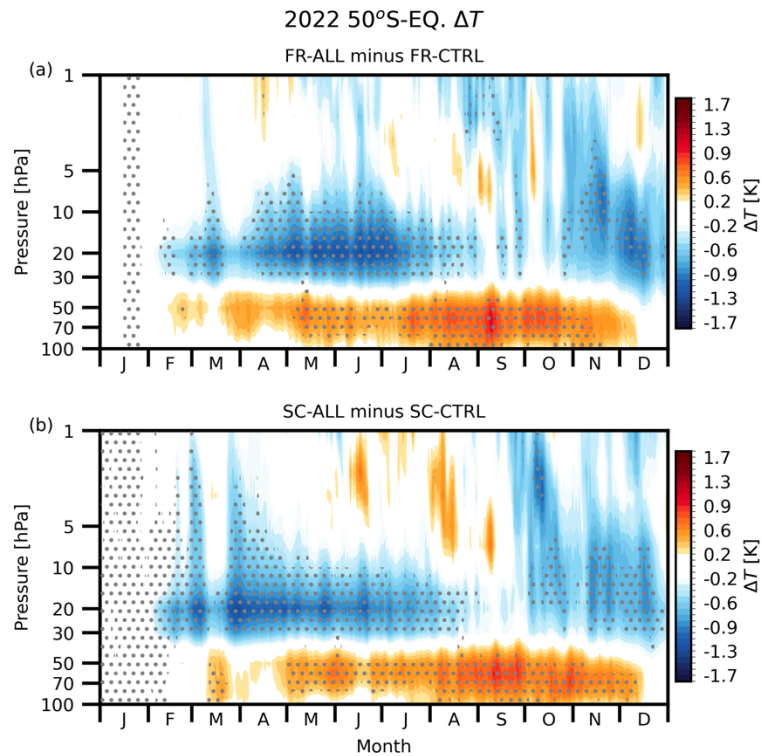
394

395

396

397

398 **Figures**

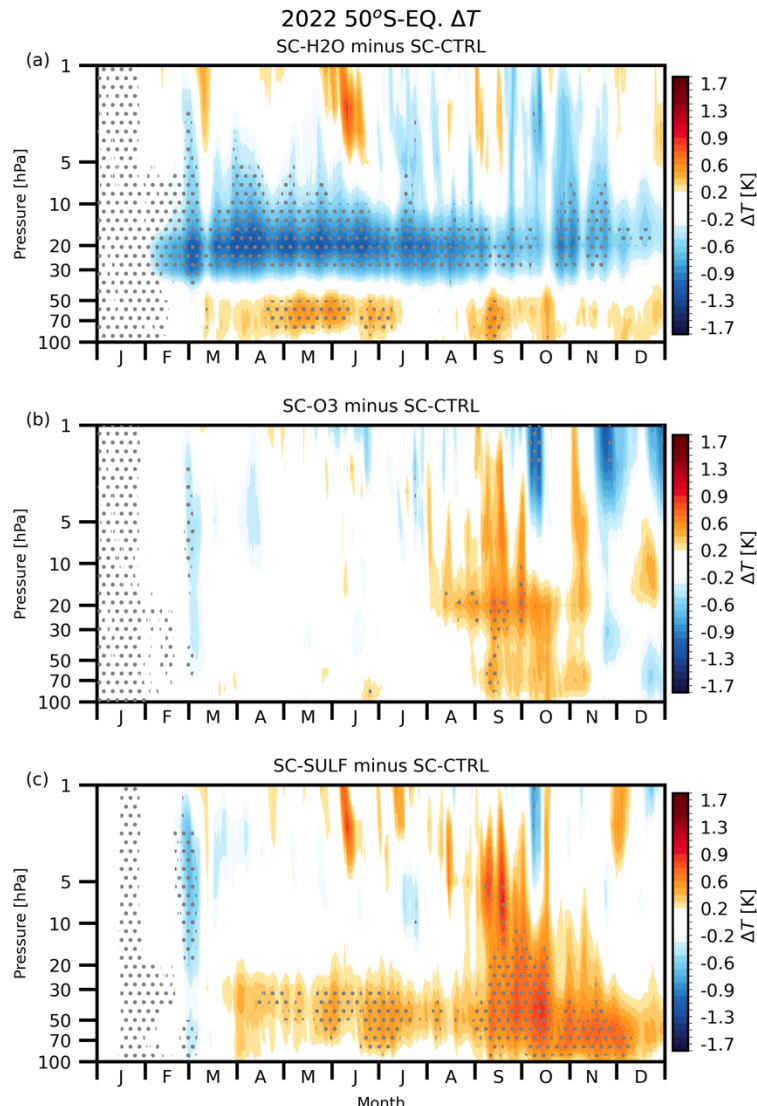


399

400 **Figure 1.** Time evolution of differences in temperature averaged over 50°S -0° between all  
401 forcing (ALL) and control (CTRL) runs, based on (a) FR and (b) SC runs, respectively. Stippling  
402 indicates statistical significance at the 95% confidence level.

403

404



405

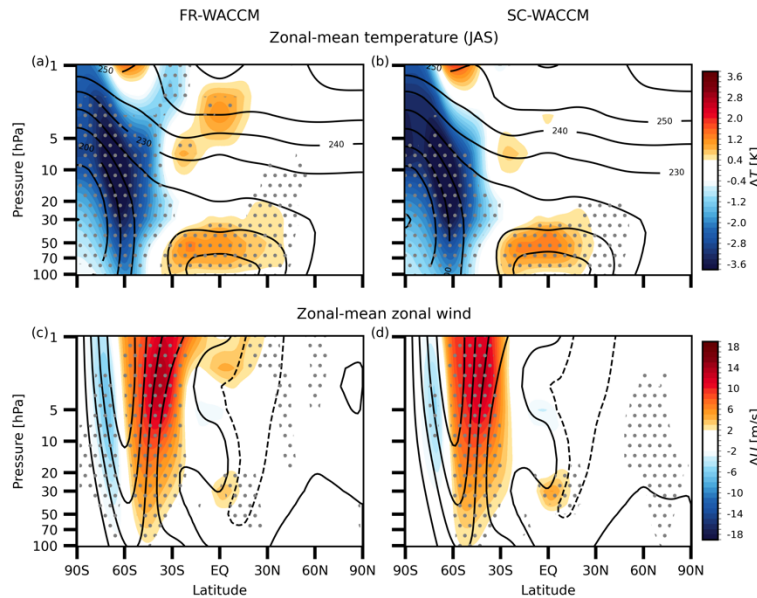
406 **Figure 2.** As in Figure 1, but for differences between (a) SC-H2O and SC-CTRL, (b) SC-O3 and  
407 SC-CTRL, and (c) SC-SULF and SC-CTRL runs.

408

409

410

411



412

413 **Figure 3.** Differences in zonal-mean (top) temperature and (bottom) zonal wind fields between  
 414 all-forcing (ALL) and control (CTRL) runs. The results are based on (left) FR and (right) SC  
 415 runs, respectively. Black line contours are spaced at 180, 190, 200... K for the mean  
 416 temperature, and -40, -20, 0... m/s for the mean zonal wind from CTRL experiments. The results  
 417 are averaged during the austral winter, from July to September 2022.

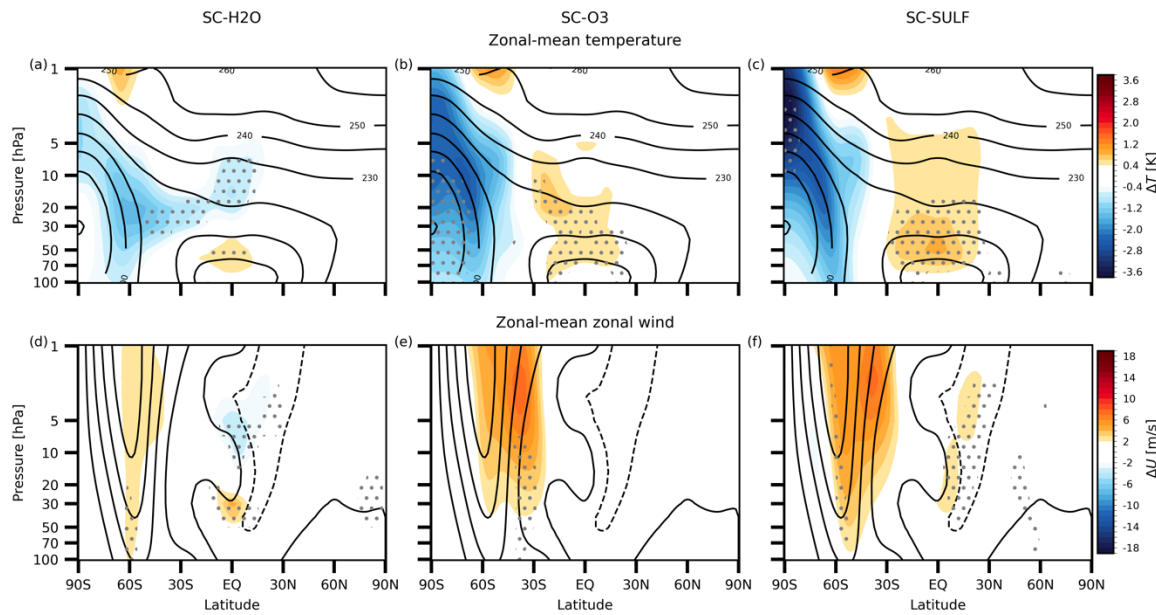
418

419

420

421

422



423

424 **Figure 4.** As in Figure 3, but for results based on (a, d) SC-H2O minus SC-CTRL, (b, e) SC-O3  
 425 minus SC-CTRL, and (c, f) SC-SULF minus SC-CTRL.

426

427

428

429

430

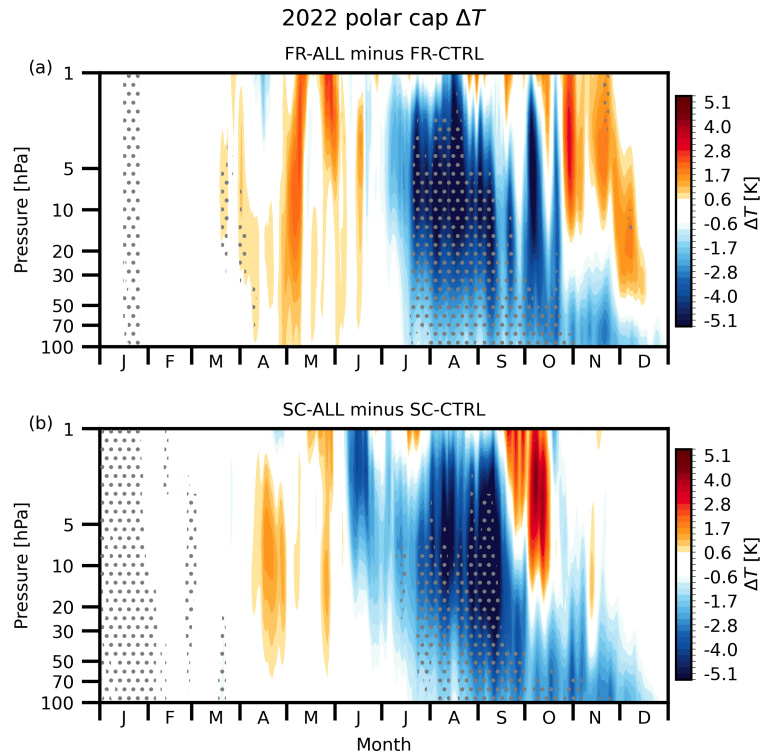
431

432

433

434

435



436

437 **Figure 5.** As in Figure. 1, bur for SH polar cap-averaged ( $60-90^{\circ}$ S) temperature.

438

439

440

441

442

443

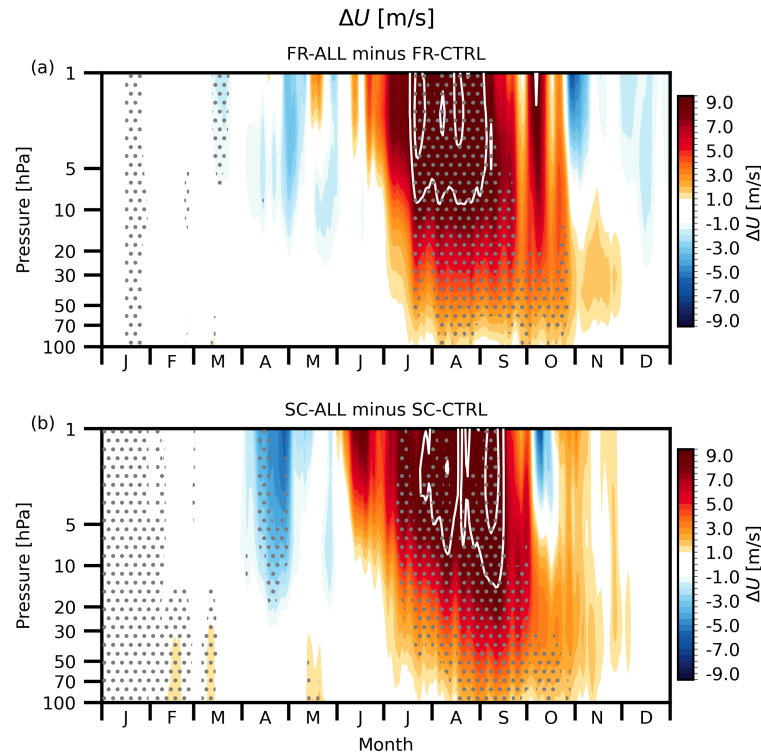
444

445

446

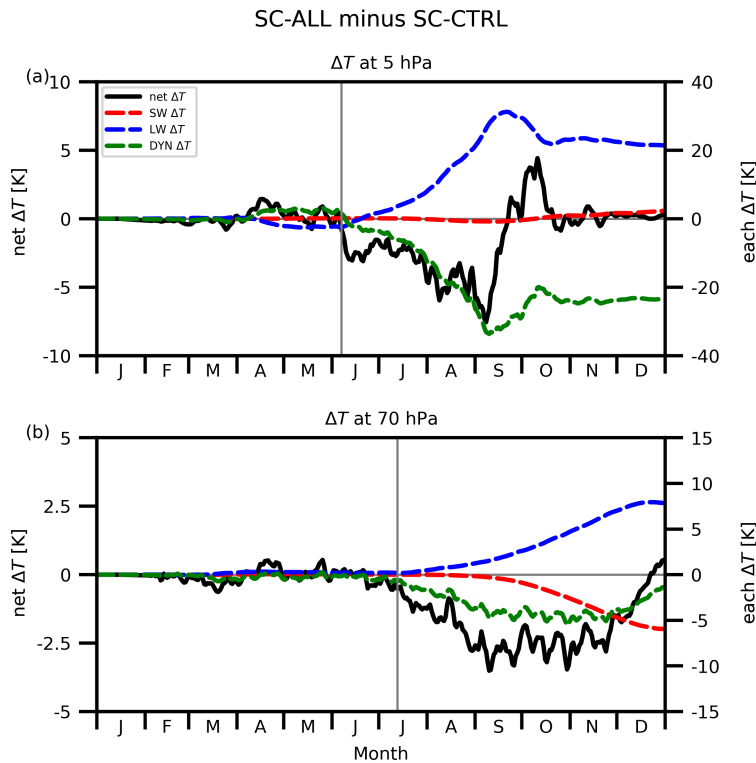
447

448



449

450 **Figure 6.** As in Fig. 5, but for zonal-wind in the SH mid-latitudes (30-60°S). White contour lines  
 451 indicate regions where zonal wind anomalies exceed 10 m/s, with intervals of 5 m/s.



452

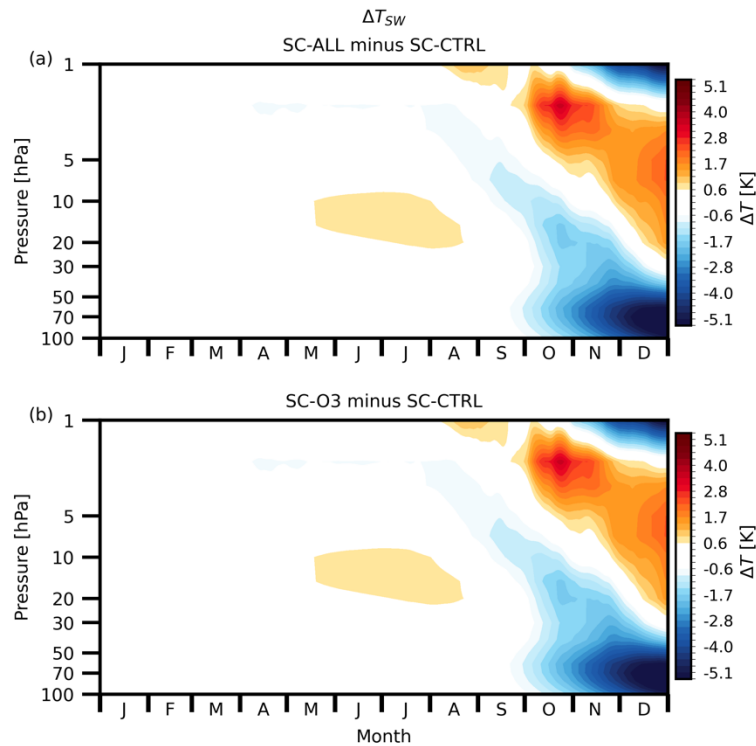
453 **Figure 7.** Time evolution of polar cap-averaged (60-90°S) temperature at (a) 5 hPa and (b) 70  
 454 hPa level. Black solid line represents net temperature change (net  $\Delta T$ ) since January 1, 2022.  
 455 Dashed lines show contribution from each of short-wave (red; SW  $\Delta T$ ), long-wave (blue; LW  
 456  $\Delta T$ ), and dynamical (green; DYN  $\Delta T$ ) processes. All results represent difference between SC-  
 457 ALL and SC-CTRL runs. The left y-axis corresponds to the net  $\Delta T$ , while the right y-axis  
 458 corresponds to the magnitude of each contribution. Grey line indicates the onset of cold  
 459 temperature anomalies and is defined as the first day when the sign of the net  $\Delta T$  changes to  
 460 negative, with the negative  $\Delta T$  value sustained for at least the next 90 days.

461

462

463

464



465

466 **Figure 8.** Time evolution of the polar cap-averaged temperature due to shortwave processes at  
467 all levels since January 1, 2022. Temperature differences between (a) SC-ALL and SC-CTRL  
468 runs, and (b) SC-O3 and SC-CTRL runs.

469

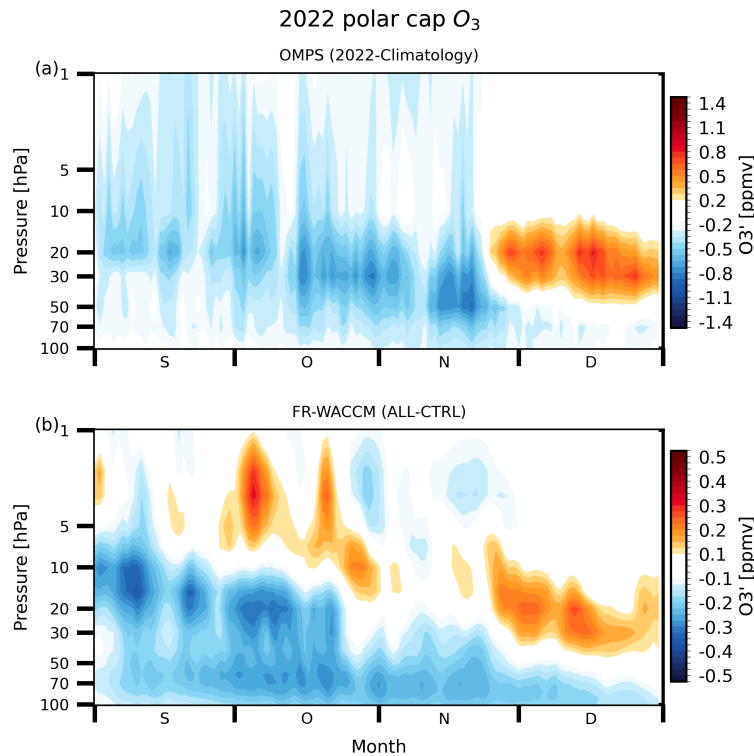
470

471

472

473

474



475

476 **Figure 9.** Springtime SH polar cap-averaged (60–90°S) ozone anomalies (with respect to the  
477 2012–2021 mean seasonal cycle) at all levels, based on (a) OMPS observations and (b) FR-  
478 WACCM (FR-ALL minus FR-CTRL).

479

480

481

482

483

484 **References**

485 Asher, E., Todt, M., Rosenlof, K., Thornberry, T., Gao, R.-S., Taha, G., et al. (2023).  
486 Unexpectedly rapid aerosol formation in the Hunga Tonga plume. *Proceedings of the National  
487 Academy of Sciences*, 120(46), e2219547120.

488 Calvo, N., Garcia, R. R., Marsh, D. R., Mills, M. J., Kinnison, D. E., & Young, P. J. (2012).  
489 Reconciling modeled and observed temperature trends over Antarctica. *Geophysical research  
490 letters*, 39(16).

491 Calvo, N., Garcia, R., & Kinnison, D. (2017). Revisiting Southern Hemisphere polar  
492 stratospheric temperature trends in WACCM: The role of dynamical forcing. *Geophysical  
493 Research Letters*, 44(7), 3402-3410.

494 Carn, S., Krotkov, N., Fisher, B., & Li, C. (2022). Out of the blue: Volcanic SO<sub>2</sub> emissions  
495 during the 2021–2022 eruptions of Hunga Tonga—Hunga Ha’apai (Tonga). *Frontiers in Earth  
496 Science*, 10, 976962.

497 Coupe, J., & Robock, A. (2021). The influence of stratospheric soot and sulfate aerosols on the  
498 Northern Hemisphere wintertime atmospheric circulation. *Journal of Geophysical Research:  
499 Atmospheres*, 126(11), e2020JD034513.

500 Coy, L., Newman, P. A., Wargan, K., Partyka, G., Strahan, S., & Pawson, S. (2022).  
501 Stratospheric circulation changes associated with the Hunga Tonga-Hunga Ha'apai eruption.  
502 *Geophysical Research Letters*, 49(22), e2022GL100982.

503 DallaSanta, K., Gerber, E. P., & Toohey, M. (2019). The circulation response to volcanic  
504 eruptions: The key roles of stratospheric warming and eddy interactions. *Journal of climate*,  
505 32(4), 1101-1120.

506 DallaSanta, K., & Polvani, L. M. (2022). Volcanic stratospheric injections up to 160 Tg (S) yield  
507 a Eurasian winter warming indistinguishable from internal variability. *Atmospheric Chemistry*  
508 and *Physics*, 22(13), 8843-8862.

509 de F. Forster, P. M., & Shine, K. P. (1999). Stratospheric water vapour changes as a possible  
510 contributor to observed stratospheric cooling. *Geophysical Research Letters*, 26(21), 3309-3312.

511 Fleming, E. L., Newman, P. A., Liang, Q., & Oman, L. D. (2024). Stratospheric temperature and  
512 ozone impacts of the Hunga Tonga-Hunga Ha'apai water vapor injection. *Journal of Geophysical*  
513 *Research: Atmospheres*, 129(1), e2023JD039298.

514 Gelaro, R., McCarty, W., Suárez, M. J., Todling, R., Molod, A., Takacs, L., et al. (2017). The  
515 modern-era retrospective analysis for research and applications, version 2 (MERRA-2). *Journal*  
516 *of climate*, 30(14), 5419-5454.

517 Gettelman, A., Mills, M., Kinnison, D., Garcia, R., Smith, A., Marsh, D., et al. (2019). The  
518 whole atmosphere community climate model version 6 (WACCM6) [software]. *Journal of*  
519 *Geophysical Research: Atmospheres*, 124(23), 12380-12403.

520 <https://doi.org/10.1029/2019JD030943>

521 Khaykin, S., Podglajen, A., Ploeger, F., Grooß, J.-U., Tencé, F., Bekki, S., et al. (2022). Global  
522 perturbation of stratospheric water and aerosol burden by Hunga eruption. *Communications*  
523 *Earth & Environment*, 3(1), 316.

524 Kodera, K. (1994). Influence of volcanic eruptions on the troposphere through stratospheric  
525 dynamical processes in the Northern Hemisphere winter. *Journal of Geophysical Research:*  
526 *Atmospheres*, 99(D1), 1273-1282.

527 Kramarova, N., Nash, E., Newman, P., Bhartia, P., McPeters, R., Rault, D., et al. (2014).  
528 Measuring the Antarctic ozone hole with the new Ozone Mapping and Profiler Suite (OMPS).  
529 Atmospheric Chemistry and Physics, 14(5), 2353-2361.  
530 Lu, J., Lou, S., Huang, X., Xue, L., Ding, K., Liu, T., et al. (2023). Stratospheric aerosol and  
531 ozone responses to the Hunga Tonga-Hunga Ha'apai volcanic eruption. *Geophysical Research*  
532 Letters, 50(4), e2022GL102315.  
533 Manzini, E., Steil, B., Brühl, C., Giorgetta, M. A., & Krüger, K. (2003). A new interactive  
534 chemistry-climate model: 2. Sensitivity of the middle atmosphere to ozone depletion and  
535 increase in greenhouse gases and implications for recent stratospheric cooling. *Journal of*  
536 *Geophysical Research: Atmospheres*, 108(D14).  
537 Millan, L., Santee, M. L., Lambert, A., Livesey, N. J., Werner, F., Schwartz, M. J., et al. (2022).  
538 The Hunga Tonga-Hunga Ha'apai hydration of the stratosphere. *Geophysical Research Letters*,  
539 49(13), e2022GL099381.  
540 Randel, W. J., Park, M., Wu, F., & Livesey, N. (2007). A large annual cycle in ozone above the  
541 tropical tropopause linked to the Brewer–Dobson circulation. *Journal of the atmospheric*  
542 *sciences*, 64(12), 4479-4488.  
543 Revell, L. E., A. Stenke, B. Luo, S. Kremser, E. Rozanov, T. Sukhodolov, and T. Peter, 2017:  
544 Impacts of Mt Pinatubo volcanic aerosol on the tropical stratosphere in chemistry–climate model  
545 simulations using CCM1 and CMIP6 stratospheric aerosol data. *Atmos. Chem. Phys.*, 17, 13  
546 139–13 150, <https://doi.org/10.5194/acp-17-13139-2017>.  
547 Rieger, L., Randel, W., Bourassa, A., & Solomon, S. (2021). Stratospheric temperature and  
548 ozone anomalies associated with the 2020 Australian New Year fires. *Geophysical Research*  
549 *Letters*, 48(24), e2021GL095898.

550 Robock, A. (2000). Volcanic eruptions and climate. *Reviews of geophysics*, 38(2), 191-219.

551 Robock, A., & Mao, J. (1995). The volcanic signal in surface temperature observations. *Journal*  
552 *of climate*, 8(5), 1086-1103.

553 Schoeberl, M., Wang, Y., Ueyama, R., Taha, G., & Yu, W. (2023). The cross equatorial transport  
554 of the Hunga Tonga-Hunga Ha'apai eruption plume. *Geophysical Research Letters*, 50(4),  
555 e2022GL102443.

556 Schoeberl, M. R., Wang, Y., Ueyama, R., Taha, G., Jensen, E., & Yu, W. (2022). Analysis and  
557 impact of the Hunga Tonga-Hunga Ha'apai stratospheric water vapor plume. *Geophysical*  
558 *Research Letters*, 49(20), e2022GL100248.

559 Sellitto, P., Podglajen, A., Belhadji, R., Boichu, M., Carboni, E., Cuesta, J., et al. (2022). The  
560 unexpected radiative impact of the Hunga Tonga eruption of 15th January 2022.  
561 *Communications Earth & Environment*, 3(1), 288. <https://doi.org/10.1038/s43247-022-00618-z>

562 Smith, K. L., Neely, R., Marsh, D., & Polvani, L. M. (2014). The specified chemistry whole  
563 atmosphere community climate model (SC-WACCM). *Journal of Advances in Modeling Earth*  
564 *Systems*, 6(3), 883-901.

565 Taha, G., Loughman, R., Colarco, P., Zhu, T., Thomason, L., & Jaross, G. (2022). Tracking the  
566 2022 Hunga Tonga-Hunga Ha'apai aerosol cloud in the upper and middle stratosphere using  
567 space-based observations. *Geophysical Research Letters*, 49(19), e2022GL100091.

568 Taha, G., Loughman, R., Zhu, T., Thomason, L., Kar, J., Rieger, L., & Bourassa, A. (2021).  
569 OMPS LP Version 2.0 multi-wavelength aerosol extinction coefficient retrieval algorithm.  
570 *Atmospheric Measurement Techniques*, 14(2), 1015-1036.

571 Toohey, M., Krüger, K., Bittner, M., Timmreck, C., & Schmidt, H. (2014). The impact of  
572 volcanic aerosol on the Northern Hemisphere stratospheric polar vortex: mechanisms and  
573 sensitivity to forcing structure. *Atmospheric Chemistry and Physics*, 14(23), 13063-13079.

574 Ueyama, R., & Wallace, J. M. (2010). To what extent does high-latitude wave forcing drive  
575 tropical upwelling in the Brewer–Dobson circulation? *Journal of the atmospheric sciences*, 67(4),  
576 1232-1246.

577 Vömel, H., Evan, S., & Tully, M. (2022). Water vapor injection into the stratosphere by Hunga  
578 Tonga-Hunga Ha'apai. *Science*, 377(6613), 1444-1447.

579 Wang, X., Randel, W., Zhu, Y., Tilmes, S., Starr, J., Yu, W., ... & Li, J. (2023). Stratospheric  
580 climate anomalies and ozone loss caused by the Hunga Tonga-Hunga Ha'apai volcanic  
581 eruption. *Journal of Geophysical Research: Atmospheres*, 128(22), e2023JD039480.

582 Witze, A. (2022). Why the Tongan eruption will go down in the history of volcanology. *Nature*,  
583 602(7897), 376-378.

584 Yook, S. (2024). Replication Data for: Figures in The Impact of 2022 Hunga Tonga-Hunga  
585 Ha'apai (Hunga) Eruption on Stratospheric Circulation and Climate [Dataset]. Harvard  
586 Dataverse. <https://doi.org/10.7910/DVN/0RGYW8>

587 Yu, P., Davis, S. M., Toon, O. B., Portmann, R. W., Bardeen, C. G., Barnes, J. E., et al. (2021).  
588 Persistent stratospheric warming due to 2019–2020 Australian wildfire smoke. *Geophysical  
589 Research Letters*, 48(7), e2021GL092609.

590 Yu, W., Garcia, R., Yue, J., Smith, A., Wang, X., Randel, W., et al. (2023). Mesospheric  
591 temperature and circulation response to the Hunga Tonga-Hunga-Ha'apai volcanic eruption.  
592 *Journal of Geophysical Research: Atmospheres*, 128(21), e2023JD039636.

593 Yulaeva, E., Holton, J. R., & Wallace, J. M. (1994). On the cause of the annual cycle in tropical  
594 lower-stratospheric temperatures. *Journal of Atmospheric Sciences*, 51(2), 169-174.

595 Zawada, D. J., Rieger, L. A., Bourassa, A. E., & Degenstein, D. A. (2018). Tomographic  
596 retrievals of ozone with the OMPS Limb Profiler: algorithm description and preliminary results.  
597 *Atmospheric Measurement Techniques*, 11(4), 2375-2393.

598 Zhang, J., Kinnison, D., Zhu, Y., Wang, X., Tilmes, S., Dube, K., & Randel, W. (2024).  
599 Chemistry contribution to stratospheric ozone depletion after the unprecedented water-rich  
600 Hunga Tonga eruption. *Geophysical Research Letters*, 51(7), e2023GL105762.

601 Zhu, Y., Bardeen, C. G., Tilmes, S., Mills, M. J., Wang, X., Harvey, V. L., et al. (2022).  
602 Perturbations in stratospheric aerosol evolution due to the water-rich plume of the 2022 Hunga-  
603 Tonga eruption. *Communications Earth & Environment*, 3(1), 248.

604 Zou, Y., Rasch, P. J., Wang, H., Xie, Z., & Zhang, R. (2021). Increasing large wildfires over the  
605 western United States linked to diminishing sea ice in the Arctic. *Nature communications*, 12(1),  
606 6048.

607